ISSN 1070-3632, Russian Journal of General Chemistry, 2015, Vol. 85, No. 6, pp. 1549–1557. © Pleiades Publishing, Ltd., 2015.
Original Russian Text © T.A. Savelieva, V.B. Loshchenov, S.A. Goryainov, L.V. Shishkina, A.A. Potapov, 2013, published in Rossiiskii Khimicheskii Zhurnal, 2013, Vol. 57, No. 5, pp. 39–47.

A Spectroscopic Method for Simultaneous Determination of Protoporphyrin IX and Hemoglobin in the Nerve Tissues at Intraoperative Diagnosis

T. A. Savelieva[a,b], V. B. Loshchenov[a,b], S. A. Goryainov[c], L. V. Shishkina[c], and A. A. Potapov[c]

[a] *Prokhorov Institute of General Physics, Russian Academy of Sciences, ul. Vavilova 38, Moscow, 119991 Russia*
e-mail: savelevat@gmail.com; loschenov@mail.ru
[b] *National Research Nuclear University MEPhI (Moscow Engineering Physics Institute), Moscow, Russia*
[c] *Burdenko Institute of Neurosurgery, Russian Academy of Sciences,*
4-ya Tverskaya-Yamskaya ul. 16, Moscow, 125047 Russia
e-mail: sergey255@yandex.ru; lshishkina@nsi.ru; aapotapoff@yandex.ru

Received February 1, 2013

Abstract—A combined method of spectroscopic analysis of biochemical and structural markers of tumor changes, including blood volume, hemoglobin oxygen saturation, protoporphyrin IX accumulation, and change in the scattering properties, was developed on the basis of the results of simulation modeling of light propagation in media with optical properties similar to those of biotissues. The method was verified on a series of optical phantoms and applied in a clinical setting for intraoperative navigation with the aim of demarcation of *glioblastoma multiforme* borders. It was shown that the method developed is superior in sensitivity and specificity to the method of video-fluorescent visualization with a Carl Zeiss OPMI Pentero microscope and can be used for demarcation of the borders of tumors exhibiting infiltrative growth.

Keywords: intraoperative diagnosis, tumors, combined spectroscopic method, fluorescence spectra, diffuse reflectance spectra, protoporphyrin IX, hemoglobin, simulation modeling, *glioblastoma multiforme*

DOI: 10.1134/S1070363215060341

INTRODUCTION

Intraoperative demarcation of cerebral glioma borders is based on intraoperative magnetic resonance imaging and ultrasonography, often combined with comparison of the intraoperative data with preoperative magnetic resonance imaging data. Along with undisputed advantages, those methods have several disadvantages. In particular, they use bulky instruments, are suitable for determining only one characteristic in one step, and employ diagnostic facilities alternately with biological tissue destruction tools. These drawbacks do not apply for video-fluorescent systems based on visualizing the distribution of fluorescent tumor marker in nerve tissues. Tumor marker most extensively used in clinical practice is protoporphyrin IX, whose accumulation in the rapidly proliferating tumor cells is induced by introduction into body of its metabolic precursor, 5-aminolevulinic acid. A disadvantage of this method is the subjective assessment of the tumor marker concentration, unacceptable in view of infiltrative tumor growth and gradual reduction of the fluorescence intensity in the perifocal zone of the tumor. In this situation, optical-spectroscopic methods, with their high speed, accuracy, and suitability for noninvasive measurments, are attractive for estimating the distribution of fluorophores in biotissue. Also, the use of the spectroscopic technique offers powerful capabilities for estimating additional parameters of biotissue status, e.g., the hemoglobin and cytochrome concentrations, which cannot be estimated with sufficient accuracy by existing visualization methods, as well as the concentration of protoporphyrin IX photoproducts, which cannot be differentiated from the fluorophore proper in video-fluorescent navigation systems. Moreover, a wide range of chromophores and fluorophores occurring in biological tissues, able of multiple light scattering on tissue and cell structures, complicates interpretation of the spectral dependences recorded.

When carried out *in vivo*, spectral analysis often combines measurement of fluorescence spectra with subsequent measurement of diffuse reflectance spectra for an object irradiated with the use of a broadband light source in order to determine its scattering properties and chromophore composition. Correction of the fluorescence spectra from analysis of diffuse reflectance spectra allows determining the fluorophore composition of the tissue. However, successive spectral measurements increase the analysis time, which may be unacceptable in clinical settings.

Here, we propose a method for simultaneous spectroscopic analysis of biological tissues based on both the fluorescence spectrum and the diffuse reflectance spectrum. In this method, the visible range of the spectrum is subdivided into three channels for recording the broadband diffuse reflectance spectrum, the laser radiation spectrum, and the fluorescence spectrum. The spectral dependences are simultaneously recorded in different modes owing to a cross-flow filtration system in the radiation sources and detector. In the short-wavelength range, biological tissues exhibit high absorption properties, which feature can be put to the best use for determining the chromophore composition of the medium, and in the long-wavelength range, predominantly light-scattering properties, which allows analyzing the structural features of tissues, as well as observing the fluorescence of exogenous fluorophores. The data interpretation is based on the results of examination of the optical properties of tissues in different states, which need to be differrentiated, with the measurement geometry taken into account.

The combined spectroscopic method proposed by us was tested at Burdenko Institute of Neurosurgery during intracranial tumor and spinal cord tumor removal surgeries [1]. Protoporphyrin IX induced by administration of 5-aminolevulinic acid served as the tumor marker. Both the sensitivity and the specificity of diagnosis with the use of the method tested were higher compared to both ordinary spectroscopic analysis and analysis of images with an Opmi Pentero system using a Blue 400 video fluorescent module in diagnosis of various types of glial tumors.

EXPERIMENTAL

Simultaneous Recording Device and Processing Algorithm for Fluorescence and Diffuse Reflectance Spectra

The spectroscopic measurements were carried out on a LESA-01-BIOSPEK (Biospek Closed Joint-Stock Company) laser spectrum analyzer with a filter placed at the outlet of the halogen lamp in order to suppress the radiation from the source outside the 500–600 nm range and a fiber-optic probe with two illumination channels.

The spectral dependences recorded and analyzed against the reference diffuse reflectance spectrum were approximated using the signal formation model described below. The purpose of this stage is to separate out the light scattering and the light absorption components of the signal. The reduced scattering coefficient served as an independent criterion for estimating the tissue density. The spectral dependence of the absorption coefficient was used to determine the concentration of the substances tested. To this end, the absorption spectrum was decomposed into known components corresponding to oxygenated and reduced forms of hemoglobin and protoporphyrin IX. In data processing we used the available published data on the visible spectra of the basic chromophores present in nerve tissue [2], as well as on the absorption and fluorescence spectra of protoporphyrin IX [3].

The signal formation model that we proposed allows recovering the data on biotissue scattering properties, which is of considerable interest in view of their changes during tumor development [4].

This model is based on analytical approximation of the dependence of the diffuse reflectance signal (backscattered radiation intensity) on the optical properties of the medium examined, obtained by simulation numerical modeling (Monte Carlo method) [5]. In this study, the Monte Carlo method was modified by taking into account the path length of light from illuminating to receiving fiber and the tissue probing depth. The histograms of distribution of these parameters were approximated by a lognormal dependence whose mode corresponded to the mean optical path length and probing depth used in searching for the analytical dependence.

Given below are the results of stochastic simulation of the efficiency of detection of the radiation diffusely reflected on the light detector, which was sent by a source with the aperture of 0.37 at the source–detector separations of 0.25, 0.5, 1, and 1.5 mm (Fig. 1a). It is seen that the absorption coefficient varies within the 0.5–8 cm^{-1} range corresponding to physiological values of normal cerebral white matter and of astrocytic tumors of various degrees of malignancy [6]. The extinction coefficient due to light scattering in the

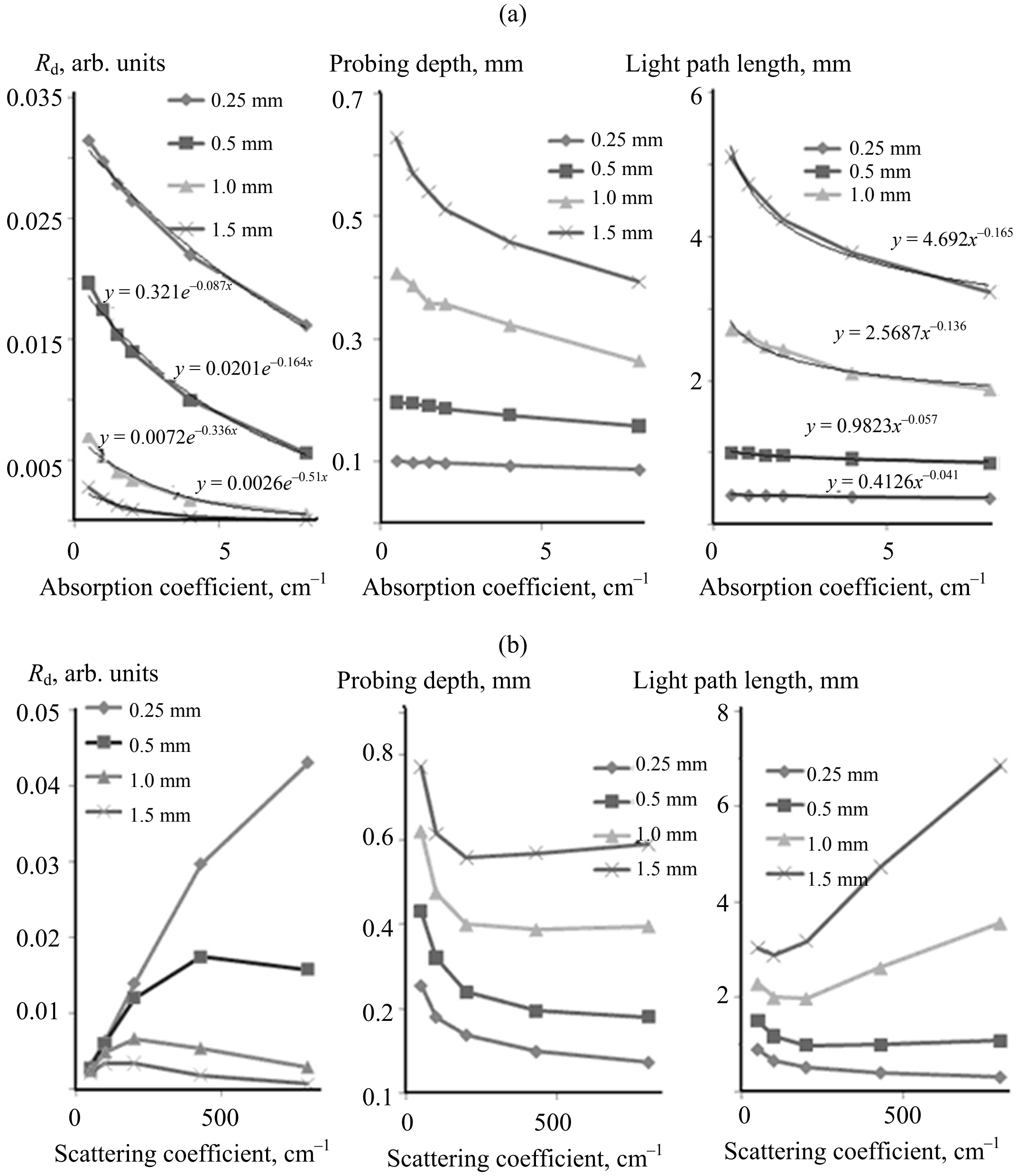

Fig. 1. Diffuse reflectance signal R_d, probing depth, and light path length in the tissue as functions of (a) absorption coefficient and (b) scattering coefficient at different light source–detector distances, obtained by numerical simulation.

medium (from here on, the scattering coefficient) and the mean cosine of the scattering angle (from here on, the scattering anisotropy factor) were taken to be equal to those of normal glial cells at the wavelength of 632.8 nm.

The stochastic simulation results include the dependences of the diffuse reflectance signal, the path length of the light between the radiation source and detector, and the tissue probing depth on the optical properties of the tissue. Obviously, all the parameters considered exhibit mainly a downward trend with increasing absorption coefficient due to the fact that the absorber molecules hinder the movement of the photons, the more often, the higher their concentration. With increasing light source–detector separation the diffuse reflectance signal tends to decrease, whereas the probing depth and the optical path length, to increase.

Approximation of the dependence of the diffuse reflectance signal R_d on the absorption coefficient μ_a

and the distance between the centers of the illuminating and receiving fibers d by a simple exponential function

$$R_d(\mu_a, d) = R_d^0(d)e^{-L(d)\mu_a} \tag{1}$$

shows that the rate of decrease of the function tends to increase linearly with increasing distance:

$$L(d) = 3.382d,$$

where R_d^0 is the diffuse reflectance signal at zero absorption coefficient, and L, trajectory length of the photons migrating in the tissue between the source and the detector.

Comparison of the dependences of the optical path length on the absorption coefficient and the rate of decrease in the diffuse reflectance function shows that, physically, this rate implies the mean free path length of photons in biotissue. Obviously, the light path length in tissue is also affected by the scattering coefficient. In this connection, we performed a similar analysis for several values of the scattering coefficient at a fixed absorption coefficient value. Figure 1b shows the simulation modeling results, which are indicative of nonmonotonic character of the dependences studied. The reason for this pattern of the dependence of the diffuse reflectance signal on the scattering coefficient is that, with increase in the light scattering coefficient, photons begin to concentrate in the area proximal (nearest) to the source; they are rescattered after traveling increasingly smaller path and, as a result, are absorbed inside an increasingly small volume. From the viewpoint of diffuse reflectance detection in a certain fixed position with respect to the light source, the monotonicity of the diffuse reflectance vs. the scattering coefficient function will inevitably be disturbed because of the dependence of the backscattered light intensity on how this position and the depth of penetration of the radiation are related. With increasing scattering coefficient the diffuse reflectance signal will decrease if the receiving fiber is located outside the area determined by the penetration depth of radiation (because this area will get increasingly closely "pressed" to the light source) and will increase if the receiving fiber is located inside the area determined by the penetration depth. It should also be noted that, with increasing scattering coefficient, the photon concentration area itself will be contracted, i.e., the relative position of this area and the radiation detector will change and the detector, in a sense, will be moving away from the light source.

The above-presented simple exponential dependence (1) takes into account a decrease in the backscattered light intensity with increasing absorption coefficient. A similar dependence on the scattering coefficient describes the behavior of the measured parameter in the distal region and does not adequately describe the behavior of this parameter in the proximal region of the illumination fiber.

For analytical description of the diffuse reflectance signal at different ratios of the scattering coefficient to the light source–detector separation we proposed a modified exponential dependence which incorporates the scattering coefficient itself, whereby the signal increase in the proximal region of the source is provided:

$$R_d = A\mu_S' e^{-(B_0 + B_1\mu_S' + B_2\mu_a)}. \tag{2}$$

Here, A and B_i are adjustable parameters which depend on the illumination and signal detection geometry, μ_S', reduced scattering coefficient defined as $\mu_S' = \mu_S\cdot(1 - g)$, g, scattering anisotropy factor, and μ_a, absorption coefficient.

Figure 2 presents the results from approximation of the dependence of the diffuse reflectance signal on the absorption coefficient and the reduced scattering coefficient by the modified exponential model (2) proposed. It is seen that the model adequately describes the behavior of the parameter of interest both in the region proximal to the light source and in the distal region and thereby is suitable for recovering the optical properties of the medium for different types of the illumination and signal detection geometry.

Verification of the Method on Optical Phantoms

The signal formation model proposed was verified on optical phantoms simulating the hemoglobin content in the nerve tissues. The scattering properties were modeled with "Lipofundin 20%" fat emulsion used in various concentrations (0.5, 2, and 8%). To simulate the blood content in the sample, human red blood cell mass was diluted with saline in the 40% proportion and introduced into the samples with the lipid emulsion to obtain 1, 2, 4, and 8% concentrations. Under presumption that the hemoglobin concentration in the simulated blood solution was 137 g/L, and hematocrit, 0.4, the concentrations obtained in the phantoms corresponded, on the average, to the concentrations of 1, 2, 4, and 8 blood milliliters per biotissue 100 g.

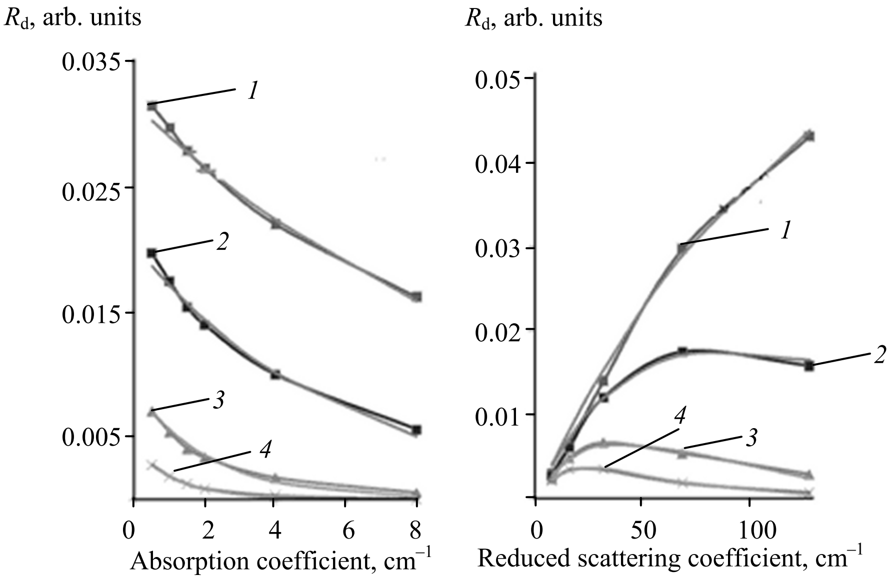

Fig. 2. Approximation by the modified exponential model proposed of the dependences of the diffuse reflectance signal R_d on the absorption coefficient and the reduced scattering coefficient, obtained in the numerical experiment for different light source–detector distances, mm: (*1*) 0.25, (*2*) 0.5, (*3*) 1, and (*4*) 1.5 are Monte Carlo simulation results, and solid lines for 0.25, 0.5, and 1 mm are modified exponential dependences.

Figure 3 shows the experimentally measured spectral dependences. Tables 1 and 2 present the results of implementation of the algorithm proposed for interpretation of the diffuse reflectance and fluorescence spectra of the optical phantoms with preset hemoglobin and lipid emulsion content in terms of the determined concentrations and the theoretical values of the optical parameters of the phantoms used.

The tissue density data obtained from analysis of the spectral dependence of the diffusely reflected radiation intensity underlie determination of the protoporphyrin IX concentration from the fluorescence index (ratio of the fluorescence intensity of the fluorophore tested to the diffusely reflected laser radiation intensity). Use in the fluorescence index calculation of the diffusely reflected laser light intensity as the normalization parameter allows eliminating the interference of the scattering properties of the biological tissue with the intensity of the fluorescence signal detected. A special correction was introduced to take into account the differences in the optical characteristics exhibited by the tissue at the excitation wavelength and in the wavelength range of fluorescent radiation [4].

Here, we examined the distribution of the spectroscopic parameters over the surgical field in patients subjected to malignant glial tumor surgery. The test group consisted of 19 patients diagnosed with glioblastoma; the distribution of bioptic materials selected for diagnosis over the tissue type was as

Table 1. Recovered scattering coefficient values μ_s', cm^{-1}

Blood content in solution, %	Fat emulsion concentration, %		
	0.5	2	8
0	8.3	38.3	122.0
1	8.2	36.1	113.7
2	8.1	34.4	114.5
4	7.7	33.5	110.0
8	7.4	32.0	111.2

Table 2. Recovered blood content values of the samples, %

Blood content in solution, %	Fat emulsion concentration, %		
	0.5	2	8
0	0.0	0.0	0.0
1	1.7	1.0	1.2
2	3.1	2.2	2.2
4	4.8	3.8	3.7
8	8.0	6.2	5.9

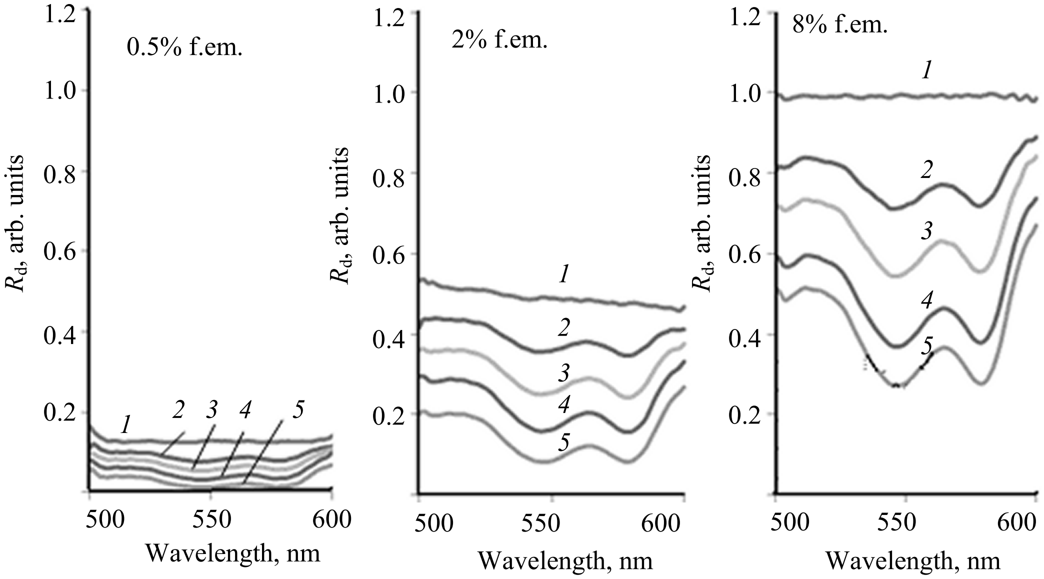

Fig. 3. Diffuse reflectance spectra of the array of optical phantoms containing a solution of red blood cell mass in fat emulsion, grouped based on the fat emulsion (f. em.) concentration. Blood content in the red blood cell mass, %: (*1*) 0, (*2*) 1, (*3*) 2, (*4*) 4, and (*5*) 8.

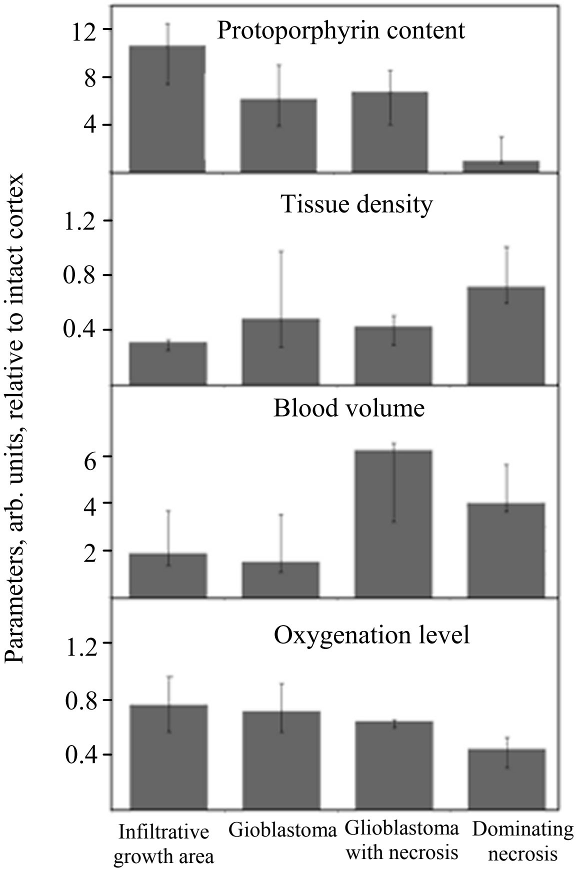

Fig. 4. Distribution of the biochemical and structural tumor markers over tumor tissue types.

follows: brain 14, infiltratitive growth area 46, glioblastoma 129, necrotic area 27.

RESULTS AND DISCUSSION

Comparison of the intraoperative *in vivo* spectroscopic analysis data for the cytoreduction area with the data for histological tissue samples taken from the same areas demonstrated correspondence of the spectroscopic characteristics examined to the tissue type.

Multiple intraoperative spectroscopic measurements revealed smooth changes for the optical characteristics in going from healthy tissue to the center of the tumor, exhibiting certain trends, as illustrated by diagrams in Fig. 4.

The tumor areas dominated by necrosis were characterized by the absence of protoporphyrin IX accumulation, high radiation scattering level and blood volume (“hemoglobin concentration”), and a low oxygenation level. The fluorescent contrast with respect to healthy cerebral cortex, exhibited by the tissue samples taken from the tumor center with microscopic necrosis inclusions, was 7 ± 1.7; the tissue density was less than half the norm; compared to the intact cerebral cortex, the blood volume was six times, on the average, higher, and the oxygenation level was at 60% of the corresponding parameter. The tissue from the center of the tumor without signs of necrosis exhibits similar characteristics, with a lower blood volume as the only exception. The infiltrated area was characterized by a protoporphyrin IX accumulation level maximum (10 ± 3 times the normal value), the lowest tissue density, the blood volume twice exceeding the normal value, and the highest level of oxygenation of the tumor tissue, close to that of the intact cerebral cortex.

Protoporphyrin IX Distribution

Selective accumulation of protoporphyrin IX in tumor tissues against the norm is a consequence of a number of enzymatic disorders [7] in rapidly prolixferating tumor cells [8]. The protoporphyrin IX content in glial brain tumors was shown to be a highly specific criterion for tumor demarcation [9], as well as for estimation of the degree of malignancy [10]. It was also demonstrated [11] that the protoporphyrin IX accumulation correlates with the proliferation index, which is responsible for a high level of this photosensitizer, observed in the actively growing regions of the tumor in the infiltrated area, as well as for its slightly lower levels at the center of the tumor and the absence of protoporphyrin IX in the necrotic area.

Structural Changes in the Tumor Tissue

When considering the structural changes in the nerve tissues, associated with glial tumor development, account should be taken of the tumor growth along myelinated nerve fibers and blood vessels without forming a capsule, which leads to infiltration of normal white cortex matter by the tumor cells [12]. At the organ tissue level of organization, glial tumors consist of the central and perifocal zones [13] and cause displacement, deviation, and destruction of nerve tracts, which processes are intensified as the tumor grows. The central zone of *glioblastoma multiforme* (the most malignant form of glial tumors) is subject to the development of necrosis in the nucleus of tumor as accompanied by destructive changes of the myelinated nerve fibers [15, 16]. The structure of tumors without necrosis at the center and without edema in the perifocal area, e.g., benign gliomas (WHO grades I–II) or anaplastic astrocytoma (WHO grade III), is typically more uniform throughout the tumor.

At the tissue level, the number and shape of cell membranes should also be taken into account. As known, the cortical white matter is by ca. 50% represented by tracts of myelinated nerve fibers comprised of multilayer membranes consisting of a lipid bilayer (70–85% dry mass) with protein inclusions (15–30%) [17, 18], which is responsible for a high refractive index of this structure. Of much importance is the surface area of the membranes of astrocytes (a kind of nervous system cells) because this parameter varies during compaction of cells in tumor and also affects the light scattering.

Thus, a decrease in the scattering coefficient for the infiltrative growth area at a high oxygenation level in blood vessels suggests that this trend can be attributed to impairment of the membrane structures of the cortex white matter. At the same time, at the center of the tumor these changes are paralleled by a decrease in oxygenation level (Warburg effect), reduction in the number of mitochondria, along with increases in the number and size of the cell nuclei. The two first-named effects lead to decreased, and the third-named effect, to increased light scattering. Thus, these processes compete against each other. The necrotic area, due to destruction of large cellular structures, exhibits an increase in the number of medium-sized scatterers, significantly affecting the scattering signal in the light source proximal area, and this may contribute to an increase in the scattering level detected. Thus, minimal scattering properties are observed at the tumor periphery, which makes this criterion the most informative in tumor demarcation.

Hemoglobin Content and Oxygenation Level in Tumor Tissues

A prognostic criterion most widely used in estimating the degree of malignancy is the change in the vascular structure and, as a consequence, in blood volume in tumor, determined typically by preoperative magnetic resonance imaging. These parameters can also be determined intraoperatively by diffuse reflectance spectroscopy, so the conclusions drawn from analysis of preoperative magnetic resonance imaging diagnosis data can be extended to the results of *in vivo* spectral analysis. The blood volume correlates with the degrees of vascularity and malignancy in gliomas [19, 20]; the microvessel density in glioma may serve as an independent prognostic factor [21, 22]; hypoxia also correlates with the degree of malignancy of tumor [23].

Wenz et al. [24] estimated the blood volume (expressed in mean ± rms terms) at 8.4 ± 2.9 and 4.2 ± 1.7 mL per tissue 100 g for cerebral gray and white matters, respectively. According to Fuss et al. [25], the same parameters are 7.2 ± 2.7 and 3.6 ± 1.5 mL per tissue 100 g, and the cerebral blood volume in astrocytomas is 6.5 ± 3.7 mL per tissue 100 g. Studies by Aronen et al. [26] showed that the ratio of the blood volume of the modified to normal tissue is 3.64 ± 1.59 for glioblastoma, whereas it is close to unity in benign tumors. Examination of the blood volume and oxygen saturation by diffuse reflectance spectroscopy in the near infrared region [27] showed that the blood volume for astrocytoma tissue is 4.96, on the average, against 18.40 mg mL^{-1} in the glioblastoma group.

Hypoxia is another important prognostic factor. Evans et al. [28] introduced several grades of hypoxia [$p(O_2)$ under physiological conditions is 10%, or 75 mmHg; hence, modest hypoxia corresponds to oxygen pressure of 2.5%, or 19 mmHg, moderate hypoxia, to 0.5%, or 4 mmHg, and severe hypoxia, to 0.1%, or 0.75 mmHg]. According to the results of intraoperative needle electrode measurements, WHO grade II tumors were characterized by modest cellular hypoxia [$p(O_2) \approx 10\%$], and grade III tumors, by modest-to-moderate hypoxia [$p(O_2) \approx 10–2.5\%$]. Severe hypoxia [$p(O_2) \approx 0.1\%$] was observed in 5 out of 12 grade IV tumors. However, Lally et al. [29] did no reveal correlation between the patient survival and the tumor hypoxia on a set of 13 patients with malignant gliomas and 10 patients with benign gliomas at an average $p(O_2)$ = 5.1 mmHg. Study of the blood volume and oxygen saturation of hemoglobin in astrocytomas of varying degrees of malignancy (13 patients), conducted by Asgari et al. [27], showed that oxygen saturation of hemoglobin in the astrocytoma group was 36% on the average against 52% in the glioblastoma group. Those data suggest significant variability of the glioblastoma tissue oxygenation compared to more homogeneous selects for the norm and benign astrocytomas, due to the heterogeneous structure of glioblastoma.

Our data are indicative of a general downward trend in hemoglobin oxygenation for the tissues in going from intact brain through the infiltrative growth area and the tumor proper to necrosis. However, this criterion is extremely sensitive to mechanical impact on tissues and can lead to underestimated oxygenation level for benign tissues.

The data on measured hemoglobin content in tumor tissues allow combining the four types of tissues tested by us into two groups, since no statistically significant differences in the blood volume were revealed between the tumor center with necroses and dominating necrosis, as well as between the tumor center and the infiltrative growth area. The two groups resulting from such combination differ by a factor of 2.5 in the hemoglobin content. These results correlate well with the above data on the blood volumes and vascular densities of various glial tumors, obtained by different measurement methods. On the whole, we can conclude that more malignant areas of tumor are characterized by higher hemoglobin levels and lower oxygenation levels compared with the tumor periphery (meant by the latter in the present case is the infiltrated area and a tumor segment showing no signs of necrosis).

CONCLUSIONS

Simulation of light propagation in media with optical properties similar to those of biological tissues allowed development of a method for spectroscopic analysis of biotissues with simultaneous quantification of tumor markers: blood volume, hemoglobin oxygen saturation, protoporphyrin IX accumulation, and change in the scattering properties. The method was verified on a series of optical phantoms containing the biochemical and structural markers of tumor changes tested or similar to them.

Application of the method as an instrument of intraoperative navigation in a clinical setting with the aim of demarcation of *glioblastoma multiforme* borders revealed the distribution patterns of the markers tested in tumor tissues.

The method exceeds the video-fluorescent visualization method based on the use of a Carl Zeiss OPMI Pentero microscope in sensitivity (88 against 78%) and specificity (82 against 60%).

The method of simultaneous spectroscopic analysis of biochemical and structural markers of tumor changes, proposed by us, is suitable for demarcation of the borders of tumors exhibiting infiltrative growth.

REFERENCES

1. Potapov, A.A. et al., *Vopr. Neirokhir.*, 2013, vol. 77, no. 2, pp. 5–12.
2. *http://omlc.ogi.edu/spectra/hemoglobin/index.html.*
3. Albani, J.R., *Structure and Dynamics of Macromolecules: Absorption and Fluorescence Studies*, Amsterdam: Elsevier, 2004.
4. Savelieva, T.A. et al., *Kratk. Soobshch. Fiz.*, 2011, no. 11, pp. 30–38.
5. Wang, L. and Jacques, S.L., *Monte Carlo Modeling of Light Transport in Multilayered Tissues in Standard C*,

Houston: University of Texas, M.D. Anderson Cancer Center, 1998.

6. *Biomedical Photonics Handbook*, Vo-Dinh, T., Ed., Boca Raton (Florida): CRC, 2003.
7. Teng, L. et al., *Brit. J. Cancer*, 2011, no. 104, pp. 798–807.
8. Ishihara, R. et al., *Neurol. Med. Chir. (Tokyo),* 2007, vol. 47, no. 2, pp. 53–57.
9. Stummer, W. et al*., J. Neurooncol*., 2008, vol. 87, pp. 103–109.
10. Gibbs-Strauss, S.L. et al., *Med. Phys*., 2009, vol. 36, pp. 974–983.
11. Valdes, P.A. et al., *Neuro-Oncology*, 2011, vol. 13, no. 8, pp. 846–856.
12. Brat, D.J., *Conf. Proc. of Am. Soc. Neuroradiol.: Integration of Imaging Strategies in Neuroradiology*, 2004, pp. 1–8.
13. Giese, A., *J. Clin. Oncol*., 2003, vol. 21, no. 8, pp. 1624–1636.
14. Tonn, J.C. and Goldbrunner, R., *Acta Neurochir. Suppl*., 2003, vol. 88, pp. 163–167.
15. Brunberg, J.A. et al., *Am. J. Neuroradiol*., 1995, vol. 16, pp. 361–371.
16. Sinha, S. et al., *Am. J. Neuroradiol*., 2002, vol. 23, pp. 520–527.
17. Johansen-Berg, H. and Behrens, T.E.-G., *Diffusion MRI: from Quantitative Measurement to in vivo Neuroanatomy*, Amsterdam: Academic, 2009, pp. 75–126.
18. Brady, S.T. et al., *Basic Neurochemistry: Principles of Molecular, Cellular, and Medical Neurobiology*, 8th ed., Amsterdam: Academic, 2011.
19. Takano, S. et al., *Cancer Res*., 1996, vol. 56, pp. 2185–2190.

20 Takahashi, J.A. et al., *J. Neurosurg*., 1992, vol. 76, pp. 792–798.

21. Scatliff, J.H. et al., *Am. J. Roentgenol. Radium Ther. Nucl. Med*., 1969, vol. 105, no. 4, pp. 795–805.
22. Weidner, N., *J. Pathol*., 1998, vol. 184, no. 2, pp. 119–122.
23. Sydney, M. et al., *Clin. Cancer Res*., 2004, vol. 15, no. 10, pp. 8177.
24. Wenz, F. et al., *Magn. Reson. Imag*., 1996, vol. 14, no. 2, pp. 157–162.
25. Fuss, M. et al., *Int. J. Radiat. Oncol. Biol. Phys*., 2000, vol. 48, no. 1, pp. 53–58.
26. Aronen, H.J. et al., *Radiology,* 1994, vol. 191, no. 1, pp. 41–51.
27. Asgari, S. et al., *Acta Neurochir*., 2003, vol. 145, no. 6, pp. 453–460.
28. Evans, S.M. et al., *Clin. Cancer Res*., 2004, vol. 10, pp. 8177–8184.
29. Lally, B.E. et al., *Cancer J*., 2006, vol. 12, no. 6, pp. 461–466.